Research Article

Journal of Environmental Nanotechnology

Green Synthesis of MgO Nanoparticles Using *Mimusops elengi* Leaf Extract: Multi-response Optimization, Machine Learning Prediction and Physicochemical Characterization

R. Karthikeyan[1*], Sobini X Pushpa[2], N. Saranya[3], F. Jessy Nirmala[4], S. Srijayanthi[5] and L. Ganesh Babu[6]

[1]Department of Automobile Engineering, Rajalakshmi Engineering College, Chennai, TN, India
[2]Department of Computer Science and Engineering, St. Xavier's Catholic College of Engineering, Nagercoil, TN, India
[3]Department of Computer Science and Business Systems, Bannari Amman Institute of Technology, Sathyamangalam, TN, India
[4]Department of Information Technology, Nandha College of Technology, Perundurai, TN, India
[5]Department of Artificial Intelligence and Data Science, R. M. K. Engineering College, Tiruvallur, TN, India
[6]Department of Robotics and Automation, Easwari Engineering College, Chennai, TN, India
Received: 31.07.2026 Accepted: 26.08.2026 Published: 30.09.2026
*karthikeyanravichandran25@gmail.com

ABSTRACT

The green production of metal oxide nanoparticles has emerged as an environmentally sustainable alternative to conventional chemical synthesis because of its simplicity, reduced chemical consumption, and lower environmental impact. Data-driven optimization techniques and machine learning algorithms have become effective tools for minimizing experimental effort while improving process efficiency. In the present study, MgO nanoparticles were synthesized using *Mimusops elengi* leaf extract, and the synthesis process was optimized by considering magnesium nitrate hexahydrate concentration, plant extract concentration, reaction temperature, and reaction time as the input variables, whereas MgO nanoparticle yield and UV–Vis absorbance were selected as the response variables. A Taguchi L27 design and ANOVA were employed to evaluate the effects of the synthesis variables, while multi-criteria decision-making and machine-learning approaches were used for optimization and predictive modelling. The tuned SVR model showed strong predictive performance, with cross-validated R^2 values of 0.9841 for MgO nanoparticle yield and 0.9955 for UV–Vis absorbance. The optimized synthesis conditions were identified as 0.14698 M magnesium nitrate hexahydrate, 4.5638% (w/v) *Mimusops elengi* leaf extract, a reaction temperature of 87.735 °C, and a reaction time of 85.905 min. Under these conditions, the predicted MgO nanoparticle yield and UV–Vis absorbance were 86.10% and 0.8332 a.u., respectively. Characterization by UV–Vis spectroscopy, XRD, and SEM confirmed the formation and crystalline nature of the synthesized MgO nanoparticles. The integrated optimization framework demonstrated that combining statistical design, multi-criteria decision-making, and machine learning provides an efficient strategy for enhancing the green synthesis of MgO nanoparticles while reducing experimental effort.

Keywords: *Mimusops elengi*; MgO nanoparticles; Taguchi optimization; Support Vector Regression (SVR); Multi-response optimization.

1. INTRODUCTION

Metal oxide nanoparticles have attracted considerable attention, because of their unique physicochemical properties and their widespread applications in biomedicine, environmental remediation, catalysis, sensors, and antimicrobial systems. Among them, magnesium oxide (MgO) nanoparticles have emerged as promising materials owing to their excellent chemical stability, biocompatibility, high surface area, and antimicrobial activity (Silva *et al.* 2022). Plant-mediated synthesis has emerged as a sustainable alternative to conventional chemical synthesis, with plant extracts providing phytochemicals that can contribute to nanoparticle formation and stabilization (Blessymol *et al.* 2023). Plant-mediated synthesis not only minimizes environmental impact but also improves nanoparticle stability through the action of naturally occurring phytochemicals. *Mimusops elengi* leaves are reported to contain polyphenolic constituents including myricitrin, myricetin, quercitrin, kaempferol derivatives, and quinic acid. These oxygen-containing phytochemicals contain hydroxyl and carbonyl functionalities that may interact with Mg^{2+} ions, influence precursor complexation and nucleation, and adsorb on developing magnesium-containing particles, thereby affecting growth and stabilization. Because the present aqueous extract was not subjected to compound-specific phytochemical

analysis, these roles are proposed from the literature rather than directly demonstrated here (Packiam *et al.* 2022). Similarly, green-synthesized MgO nanoparticles using Allium cepa and Malus domestica leaf extracts exhibited crystallite sizes of 12–20 nm, enhanced antioxidant and antibacterial activities, and effective antimicrobial performance, highlighting the versatility of plant-assisted MgO nanoparticle synthesis (Periakaruppan *et al.* 2025a; Tariq *et al.* 2026). Olea europaea leaf-mediated magnesium oxide nanoparticles (MgO NPs) were green synthesized, producing polycrystalline cubic nanoparticles with a crystallite size of 12.08 nm, an average particle size of 28.13 nm, confirming the effectiveness of plant-assisted synthesis for stable MgO nanomaterials (Ulwali *et al.* 2021). Vernonia amygdalina leaf-mediated magnesium oxide nanoparticles (MgO NPs) were green synthesized by varying the magnesium nitrate hexahydrate precursor concentration (0.1–0.4 M), producing crystalline nanoparticles with an average crystallite size of 11.94 nm (Tero *et al.* 2026). Despite progress in plant-assisted MgO synthesis, reproducibly identifying synthesis conditions that simultaneously provide high product recovery and consistent optical response remains challenging. In particular, limited studies have integrated structured experimental design, objective multi-response ranking, and comparative machine-learning prediction for MgO synthesis using *Mimusops elengi*. This unresolved methodological gap motivates the integrated optimization framework adopted in the present study.

Plant-mediated MgO synthesis has increasingly focused on controlling precursor concentration, extract composition, temperature, and reaction duration because these parameters influence nucleation, precursor conversion, particle stabilization, and final physicochemical characteristics (Jeevanandam *et al.* 2017). Previous MgO studies using *Allium cepa*, *Malus domestica*, *Olea europaea*, and *Vernonia amygdalina* extracts demonstrate the feasibility of plant-assisted MgO formation, but systematic multi-response optimization and predictive comparison remain comparatively limited. Likewise, hydrotalcite–silver nanoparticles synthesized using Syzygium nervosum leaf extract achieved a 77.54% reduction yield and excellent antibacterial activity through Response Surface Methodology (RSM) optimization (Thai *et al.* 2024), while hydrotalcite–zinc–silver nanoparticles prepared using Piper betle extract reached 62.12% synthesis efficiency with strong antibacterial performance (Anh *et al.* 2025). Green-synthesized carbon dots derived from *Murraya koenigii* integrated with reduced graphene oxide also demonstrated excellent electrochemical sensing performance, achieving a limit of detection of 0.21 mM for creatinine detection (Roy *et al.* 2025). Furthermore, MgO-doped rice husk biochar composites synthesized through green chemistry exhibited maximum pesticide adsorption capacities of 115.64, 89.47, and 78.73 μg mg^{-1}, confirming the growing importance of sustainable nanomaterials for environmental remediation (Kar *et al.* 2025).

Although green synthesis has become increasingly established, identifying the optimum synthesis conditions remains a major challenge because nanoparticle formation is simultaneously influenced by precursor concentration, plant extract concentration, reaction temperature, and reaction time. Consequently, statistical optimization techniques have been widely adopted to reduce experimental effort while improving synthesis efficiency. Response Surface Methodology coupled with Central Composite Design (CCD) has successfully optimized silver nanoparticle synthesis using *Chromolaena odorata* leaf extract (Ogunsile *et al.* 2024), whereas Box–Behnken Design (BBD) has been effectively applied for optimizing hydrotalcite-supported silver nanoparticle synthesis. Beyond synthesis optimization, statistical approaches have also been employed to optimize engineering systems, including Spirulina biodiesel blended with green-synthesized CeO_2 nanoparticles using RSM–CCD, which achieved a minimum specific fuel consumption of 0.275 kg kWh^{-1} while significantly reducing CO emissions (Gomkale *et al.* 2026). Similarly, Taguchi and Analysis of Variance (ANOVA) successfully optimized Cordia dichotoma/nano-alumina epoxy nanocomposites, where fiber content contributed approximately 90% toward mechanical performance (Edlabadkar *et al.* 2025). Multi-criteria decision-making techniques such as CRITIC, CODAS, and MARCOS have also demonstrated superior capability in simultaneously optimizing multiple performance characteristics of hybrid composites (Gomkale *et al.* 2025).

The primary objective of this study is to optimize plant-assisted MgO nanoparticle synthesis using *Mimusops elengi* leaf extract and obtain reproducible synthesis conditions providing high MgO recovery and consistent optical characteristics. Four synthesis variables magnesium nitrate concentration (0.05–0.15 M), extract concentration (2–8% w/v), reaction temperature (60–90 °C), and reaction time (30–90 min) were investigated. Taguchi–ANOVA was used to quantify process effects, LEBM–MARCOS to evaluate the two responses simultaneously, and ANN, LSBoost, and SVR to compare predictive performance and identify a model suitable for continuous optimization. The proposed framework aims to simultaneously maximize nanoparticle yield and UV–Vis absorbance while identifying the most accurate predictive model, thereby providing a reliable, efficient, and sustainable strategy for green nanomaterial synthesis. MgO nanoparticle yield was selected to represent process recovery, whereas UV–Vis absorbance was used as a standardized comparative optical response associated with the synthesized material. Absorbance was not treated as a direct measure of particle size, purity, or nanoparticle quality because it can depend on concentration, dispersion state, aggregation,

and optical path length. Accordingly, all samples were evaluated under identical dispersion, sample-volume, cuvette-path-length, wavelength, and instrumental conditions. Each method addresses a different stage of the optimization problem. The Taguchi L27 design structures the 27 synthesis experiments and evaluates four factors at three levels; ANOVA quantifies their statistical contributions; LEBM assigns objective importance to yield and absorbance; MARCOS ranks the discrete experimental alternatives; and ANN, LSBoost, and SVR model nonlinear input–response relationships and enable predictive comparison.

2. MATERIALS AND METHODS

2.1 Selection of Plant Material

Fresh leaves of *Mimusops elengi*, a medicinal plant recognized for its rich phytochemical composition, were selected as a plant-derived source for the green synthesis of MgO nanoparticles. Leaf samples were collected from the Sathyamangalam Reserve Forest, Sathyamangalam, Erode district, Tamil Nadu, India. The collected material was transported to the laboratory in clean polyethylene bags for subsequent processing and nanoparticle synthesis.

2.2 Preparation of *Mimusops elengi* Leaf Extract

Freshly collected *Mimusops elengi* leaves were thoroughly washed with deionized water to remove surface impurities and then air-dried under ambient conditions for 7 days in the dark and protected from direct sunlight (Hossain *et al.* 2024). The dried leaves were ground into a fine powder using a laboratory grinder and sieved through a 1 mm mesh to obtain a uniform particle size. Aqueous leaf extracts corresponding to 2%, 5%, and 8% (w/v) were prepared based on the initial dried leaf-material-to-solvent ratio. Accordingly, 2, 5, and 8 g of powdered leaf material were separately mixed with 100 mL of deionized water to prepare the respective extract concentrations. Each mixture was heated at 60 °C for 3 h in a water bath to extract the bioactive phytochemicals. After cooling to ambient temperature, the mixtures were separately filtered through Whatman No. 1 filter paper. Thus, the 2%, 5%, and 8% (w/v) extract concentrations used in the Taguchi design represent the mass of dried leaf material extracted per 100 mL of deionized water and not dilution or concentration of a 5% stock extract. The final filtrate volume was adjusted to 100 mL with deionized water, and the measured pH of the extracts was 6.5. The extracts were freshly prepared for each experimental batch and used within 24 h. The resulting clear filtrates were subsequently used for the green synthesis of MgO nanoparticles.

2.3 Green Synthesis of MgO Nanoparticles

MgO nanoparticles were synthesized through an environmentally benign approach using *Mimusops elengi* leaf extract as a plant-derived complexing and stabilizing medium. An aqueous solution of magnesium nitrate hexahydrate was prepared as the magnesium precursor, and its concentration was adjusted according to the Taguchi L27 experimental design (Periakaruppan *et al.* 2025b). The prepared *Mimusops elengi* leaf extract was added dropwise to the precursor solution under continuous magnetic stirring to ensure homogeneous mixing. The synthesis parameters, including magnesium nitrate hexahydrate concentration (0.05–0.15 M), plant extract concentration (2–8% w/v), reaction temperature (60–90 °C), and reaction time (30–90 min), were systematically varied according to the experimental design matrix.

During this process, the *Mimusops elengi* leaf extract acted primarily as a plant-derived complexing and stabilizing medium. Its phytochemical constituents may interact with Mg^{2+} ions and influence complexation, nucleation, precipitation, stabilization, and morphology of the magnesium-containing precursor. The progression of the synthesis was monitored by UV–Vis spectroscopy over a wavelength range of 250–600 nm. Absorbance spectra were recorded after 1, 2, and 4 h of reaction to evaluate time-dependent changes in optical absorption. A broad absorption maximum was observed at approximately 375–380 nm and was used to evaluate the optical response. Following recovery and drying of the magnesium-containing intermediate, subsequent calcination at 450 °C for 2 h promoted its thermal conversion into crystalline MgO nanoparticles.

Following completion of the reaction, the suspension was centrifuged at 10,000 rpm for 20 min to recover the precipitated product. The collected precipitate was washed repeatedly with distilled water to remove residual precursor ions and phytochemical constituents. The purified product was then dried in a hot-air oven at 80 °C for 12 h. The material obtained after centrifugation, washing, and drying is herein referred to as the dried magnesium-containing intermediate. This intermediate was subsequently calcined in a muffle furnace at 450 °C for 2 h using a heating rate of 5 °C min^{-1} under an air atmosphere. After calcination, the sample was allowed to cool naturally to room temperature inside the furnace. The calcined product is herein referred to as the final MgO nanoparticles (Ramadhan and Ahmed, 2026).

The synthesized MgO nanoparticle powder was stored in airtight containers and subsequently characterized using UV–Vis spectroscopy, X-ray diffraction (XRD) and scanning electron microscopy (SEM). UV–Vis spectra were recorded over a wavelength range of 250–600 nm to investigate the optical

characteristics. XRD patterns were recorded over a 2θ range of 10–80° to determine the crystalline structure and phase composition. Surface morphology was examined using a ZEISS scanning electron microscope operated at an accelerating voltage of 3.00 kV and a working distance of 6.6 mm. SEM images were acquired using an SE2 detector at magnifications of 4.00 k× and 20.00 k× (Prisrin *et al.* 2022).

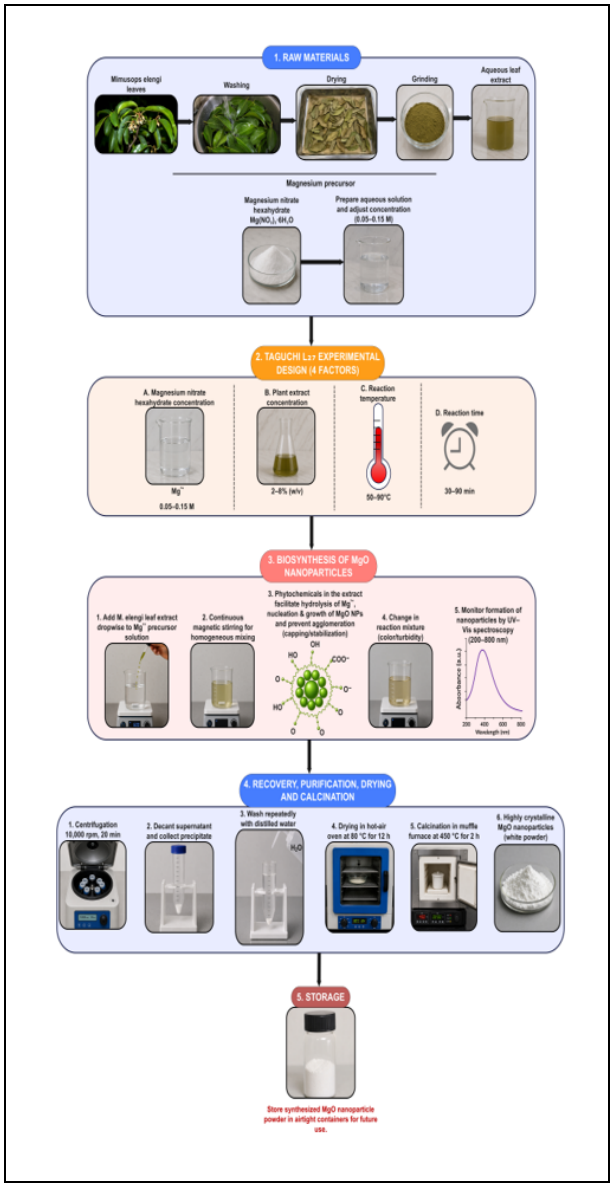

Fig. 1: Workflow for green synthesis of MgO nanoparticles by *Mimusops elengi* leaf extract

2.4 Experimental Design Using Taguchi Method

The synthesis parameters of MgO nanoparticles were designed using a Taguchi orthogonal array to reduce the number of experiments while maintaining sufficient information for statistical analysis. Four process variables, namely magnesium nitrate hexahydrate concentration (A), *Mimusops elengi* leaf extract concentration (B), reaction temperature (C), and reaction time (D), were selected as the control factors.

Table 1. Factor levels employed in the Taguchi design

Factor	Parameter	Level 1	Level 2	Level 3
A	$Mg(NO_3)_2{\cdot}6H_2O$ concentration (M)	0.05	0.10	0.15
B	Plant extract concentration (% w/v)	2	5	8
C	Reaction temperature (°C)	60	75	90
D	Reaction time (min)	30	60	90

An L27 (3^4) orthogonal array consisting of 27 experimental trials was selected to evaluate four synthesis factors at three levels. The Taguchi design was primarily employed to estimate the main effects of magnesium nitrate hexahydrate concentration, *Mimusops elengi* extract concentration, reaction temperature, and reaction time. Factor interactions were not deliberately assigned to specific columns of the orthogonal array and were therefore not independently estimated. Each of the 27 Taguchi conditions was evaluated as an individual experimental run, while triplicate experiments were performed separately to confirm the final SVR-predicted optimum.

2.5 Analysis of Variance

Analysis of variance was carried out to analyse the statistical significance of all synthesis parameters on MgO nanoparticle yield and UV–Vis absorbance. Significance of the model and individual factors was evaluated at a confidence level of 95% (Babu *et al.* 2026).

The F-ratio was calculated as:

$$F = \frac{MS_{\text{Factor}}}{MS_{\text{Error}}} \quad \ldots (1)$$

Where,

$$MS = \frac{SS}{DF} \quad \ldots (2)$$

The percentage contribution of each factor was calculated as

$$P_i = \frac{SS_i}{SS_T} \times 100 \quad \ldots (3)$$

Where,

SS_i represents the sum of squares of the ith factor,

SS_T denotes the total sum of squares.

Factors with $p < 0.05$ were considered statistically significant.

2.6 Multi-Criteria Decision-Making (MCDM)

Because MgO nanoparticle synthesis involves simultaneous optimization of more than one response, multi-criteria decision-making techniques were used to determine the best experimental condition. MgO nanoparticle yield and UV–Vis absorbance were considered as beneficial criteria, where higher values indicate superior nanoparticle synthesis performance.

The experimental decision matrix can be expressed as

$$X = [x_{ij}]_{m\times n} \quad \dots (4)$$

Where,

m denotes number of experimental runs,

n denotes number of response criteria.

2.6.1 LEBM Method

The decision matrix was first normalized using benefit-type normalization (Altıntaş, 2025),

$$r_{ij} = \frac{x_{ij}}{\max(x_j)} \quad \dots (5)$$

The weighted normalized matrix was obtained as

$$v_{ij} = w_j r_{ij} \quad \dots (6)$$

Where,

$$\sum_{j=1}^{n} w_j = 1 \quad \dots (7)$$

The Euclidean distance of all alternative from ideal solution was computed as

$$D_i = \sqrt{\sum_{j=1}^{n} \left(v_{ij} - v_j^+\right)^2} \quad \dots (8)$$

The alternatives were ranked according to the minimum distance from the ideal solution.

2.6.2 MARCOS Method

Measurement Alternatives and Ranking according to Compromise Solution (MARCOS) were employed to rank all experimental alternatives (Khanam *et al.* 2024).

The decision matrix was expanded by introducing ideal (AI) and anti-ideal (AAI) solutions.

The normalized matrix was calculated as,

For benefit criteria,

$$n_{ij} = \frac{x_{ij}}{x_{AI}} \quad \dots (9)$$

The weighted normalized matrix was obtained as

$$v_{ij} = n_{ij} w_j \quad \dots (10)$$

The utility degree was determined by,

$$K_i^- = \frac{S_i}{S_{AAI}} \quad \dots (11)$$

$$K_i^+ = \frac{S_i}{S_{AI}} \quad \dots (12)$$

Where,

$$S_i = \sum_{j=1}^{n} v_{ij} \quad \dots (13)$$

Finally, the utility function was calculated as,

$$f(K_i) = \frac{K_i^+ + K_i^-}{1 + \frac{1-K_i^+}{K_i^+} + \frac{1-K_i^-}{K_i^-}} \quad \dots (14)$$

The experimental run with the highest utility value was identified as the best discrete experimental run.

2.7 Machine Learning Models

Three ML algorithms were employed to establish predictive relationships between the synthesis parameters and the response variables.

The input variables were,

$$X = [A, B, C, D] \quad \dots (15)$$

Where,

$A = Mg(NO_3)_2 \cdot 6H_2O$ concentration,

B = *Mimusops elengi* extract concentration,

$C =$ reaction temperature,

$D =$ reaction time.

The response variables were

$$Y = [Y_1, Y_2] \quad \dots (16)$$

Where,

$Y_1 = MgO$ nanoparticle yield (%),

$Y_2 = UV - Vis$ absorbance.

Five-fold cross-validation was employed to evaluate prediction performance. Models were assessed by the coefficient of determination (R^2), root mean

square error (RMSE), mean absolute error (MAE), and mean absolute percentage error (MAPE). Considering the limited dataset of 27 experimental observations, this cross-validation strategy was used to reduce the risk of overfitting and provide a more robust assessment of predictive performance. In particular, ANN performance was evaluated using cross-validated R^2, RMSE, MAE, and MAPE rather than relying solely on full-dataset fitting. Nevertheless, the relatively small dataset limits broader model generalizability, and validation using a larger independent dataset is recommended for future studies.

Prior to model development, the input and output variables were normalized to the range of 0–1 using min–max normalization to account for differences in their numerical scales. During five-fold cross-validation, the normalization parameters were determined exclusively from the training data within each fold and subsequently applied to the corresponding validation data. Hyperparameter tuning was also performed using only the training data within each cross-validation iteration to prevent data leakage. Model predictions were transformed back to their original scales before calculating R^2, RMSE, MAE, and MAPE.

Statistical indices were calculated as (Jang *et al.* 2026).

$$R^2 = 1 - \frac{\sum (y_i - \hat{y}_i)^2}{\sum (y_i - \bar{y})^2} \quad \ldots (17)$$

$$RMSE = \sqrt{\frac{1}{n}\sum (y_i - \hat{y}_i)^2} \quad \ldots (18)$$

$$MAE = \frac{1}{n}\sum |y_i - \hat{y}_i| \quad \ldots (19)$$

$$MAPE = \frac{100}{n}\sum \left|\frac{y_i - \hat{y}_i}{y_i}\right| \quad \ldots (20)$$

2.7.1 Artificial Neural Network (ANN)

A feed-forward ANN trained using resilient backpropagation was developed to model the nonlinear relationships between the synthesis variables and responses (Sonya *et al.* 2025). The optimized architecture consisted of four input neurons, one hidden layer containing six neurons, and two output neurons representing MgO nanoparticle yield and UV–Vis absorbance. The hidden layer employed a hyperbolic tangent sigmoid (tansig) activation function, while the output layer used a linear (purelin) activation function. The number of hidden neurons was selected by evaluating candidate network architectures with different hidden-layer sizes, and the six-neuron configuration was selected based on the lowest cross-validation prediction error. Model performance was evaluated using five-fold cross-validation.

2.7.2 Least-Squares Boosting (LSBoost)

Least-Squares Boosting (LSBoost) regression was implemented using regression trees as weak learners. Separate LSBoost models were developed for MgO nanoparticle yield and UV–Vis absorbance. The models consisted of 100 boosting learners with a learning rate of 0.1 and a minimum leaf size of 5. The least-squares loss function was employed during sequential boosting. Hyperparameters were selected based on the lowest cross-validation prediction error using five-fold cross-validation. The optimized models were subsequently used to predict the respective responses.

2.7.3 Support Vector Regression

Separate Support Vector Regression (SVR) models with a Gaussian kernel function were developed to predict MgO nanoparticle yield and UV–Vis absorbance. The principal SVR hyperparameters, including the box constraint (C), epsilon (ε), and kernel scale, were tuned using five-fold cross-validation. Hyperparameter combinations were evaluated based on cross-validation prediction errors, and the combination providing the lowest error was selected separately for each response. Following hyperparameter tuning, the final SVR models were trained using the complete dataset. Model performance was evaluated using R^2, RMSE, MAE, and MAPE. Separate response-specific SVR models were employed because yield and absorbance have different numerical scales and response characteristics. SVR exhibited the strongest overall cross-validated predictive performance compared with ANN and LSBoost and was therefore selected for final process optimization.

2.8 Process Optimization and Experimental Validation

The optimized SVR model was employed for simultaneous optimization of MgO nanoparticle yield and UV- Vis absorbance using the desirability function approach. Equal weights were assigned to both responses.

The individual desirability function was calculated as

$$d_i = \frac{Y_i - Y_{\min}}{Y_{\max} - Y_{\min}} \quad \ldots (21)$$

The overall desirability was determined by the weighted geometric mean

$$D = \left(d_1^{w_1} d_2^{w_2}\right) \quad \ldots (22)$$

Where,

$$w_1 + w_2 = 1 \quad \ldots (23)$$

The SVR-predicted optimum synthesis parameters corresponded to the maximum desirability value. Confirmation experiments were subsequently performed under the predicted optimum conditions, and the prediction error was calculated using eqn (24)

$$\text{Prediction Error} = \left|\frac{\text{Experimental} - \text{Predicted}}{\text{Experimental}}\right| \times 100 \quad \ldots (24)$$

3. RESULTS AND DISCUSSION

3.1 Taguchi Experimental Results

Effects of magnesium nitrate hexahydrate concentration, *Mimusops elengi* leaf-extract concentration, reaction time, and reaction temperature on MgO NPs yield and UV–Vis absorbance were evaluated using an L27 Taguchi orthogonal design. The experimental responses are presented in Table 2.

MgO nanoparticle yield varied from 40.00 to 85.33%, while UV–Vis absorbance ranged from 0.469 to 0.829 a.u. The lowest responses were observed at 0.05 M magnesium nitrate, 2% extract, 60 °C, and 30 min. In contrast, the highest experimental yield and absorbance were obtained in run 9 at 0.15 M magnesium nitrate, 8% extract, 90 °C, and 90 min.

The simultaneous increase in yield and absorbance suggests that conditions favoring greater MgO formation also produced a stronger optical response. Nevertheless, the effect of plant-extract concentration was nonlinear, indicating that excessive extract concentration did not always improve nanoparticle formation.

Table 2. Taguchi experimental results for MgO nanoparticle synthesis

Run	$Mg(NO_3)_2 \cdot 6H_2O$ (M)	*M. elengi* Extract (% w/v)	Temperature (°C)	Time (min)	MgO Yield (%)	UV–Vis Absorbance (a.u.)
1	0.05	2	60	30	40.00	0.469
2	0.10	2	60	30	47.86	0.528
3	0.15	2	60	30	55.77	0.591
4	0.05	5	75	60	60.03	0.628
5	0.10	5	75	60	70.25	0.702
6	0.15	5	75	60	81.24	0.790
7	0.05	8	90	90	59.05	0.626
8	0.10	8	90	90	71.99	0.730
9	0.15	8	90	90	85.33	0.829
10	0.05	2	75	90	55.05	0.584
11	0.10	2	75	90	66.58	0.677
12	0.15	2	75	90	78.37	0.769
13	0.05	5	90	30	61.08	0.643
14	0.10	5	90	30	70.74	0.718
15	0.15	5	90	30	82.98	0.814
16	0.05	8	60	60	48.23	0.526
17	0.10	8	60	60	57.51	0.598
18	0.15	8	60	60	67.53	0.676
19	0.05	2	90	60	56.98	0.617
20	0.10	2	90	60	68.71	0.704
21	0.15	2	90	60	81.06	0.800
22	0.05	5	60	90	58.39	0.601
23	0.10	5	60	90	69.68	0.683
24	0.15	5	60	90	79.43	0.764
25	0.05	8	75	30	49.68	0.556
26	0.10	8	75	30	59.88	0.626
27	0.15	8	75	30	69.04	0.703

3.2 Main Effects of Synthesis Parameters

The correct factor-level means calculated from the MgO experimental dataset are summarized in Table 3.

Table 3. Factor-level means for MgO nanoparticle yield

Factor	Level 1	Level 2	Level 3	Delta	Rank
$Mg(NO_3)_2 6H_2O$ concentration	54.28	64.80	75.64	21.36	1
Plant-extract concentration	61.15	70.42	63.14	9.27	3
Reaction temperature	58.27	65.57	70.88	12.61	2
Reaction time	59.67	65.73	69.32	9.65	4

The magnesium nitrate concentration exerted the largest effect on nanoparticle yield. Raising the precursor concentration from 0.05 to 0.15 M increased average yield from 54.28 to 75.64%. A greater precursor concentration provides more magnesium ions for hydrolysis and subsequent MgO formation.

Reaction temperature was the second most influential parameter. The mean yield increased from 58.27% at 60 °C to 70.88% at 90 °C. Higher temperature likely enhanced precursor hydrolysis, molecular collision frequency, nucleation, and conversion of magnesium-containing intermediates.

The plant-extract concentration showed a peaked response. Increasing the extract level from 2 to 5% w/v improved the mean yield from 61.15 to 70.42%, whereas further increasing it to 8% reduced the mean to 63.14%. This behavior may arise from an optimum concentration of phytochemicals required for complexation, stabilization, and nucleation. At excessive extract concentrations, organic constituents may cover the growing particles, increase solution viscosity, or limit effective precursor interaction.

Longer reaction time generally improved yield, increasing the mean value from 59.67% at 30 min to 69.32% at 90 min. The improvement suggests that extended reaction time permitted more complete precursor conversion and particle formation.

Table 4. Factor-level means for UV–Vis absorbance

Factor	Level 1	Level 2	Level 3	Delta	Rank
$Mg(NO_3)_2 \cdot 6H_2O$ concentration	0.5833	0.6629	0.7484	0.1651	1
Plant-extract concentration	0.6377	0.7048	0.6522	0.0671	3
Reaction temperature	0.6040	0.6706	0.7201	0.1161	2
Reaction time	0.6276	0.6712	0.6959	0.0683	4

The absorbance response followed a pattern comparable to nanoparticle yield. The precursor concentration produced the largest difference between factor levels, followed by temperature. The maximum average absorbance was observed at 0.15 M magnesium nitrate, 5% extract, 90 °C, and 90 min.

Main effects plots showing the influence of $Mg(NO_3)_2 \cdot 6H_2O$ concentration, *Mimusops elengi* leaf extract concentration, reaction temperature, and reaction time on the mean MgO nanoparticle yield obtained from the Taguchi L27 experimental design were shown in fig. 2.

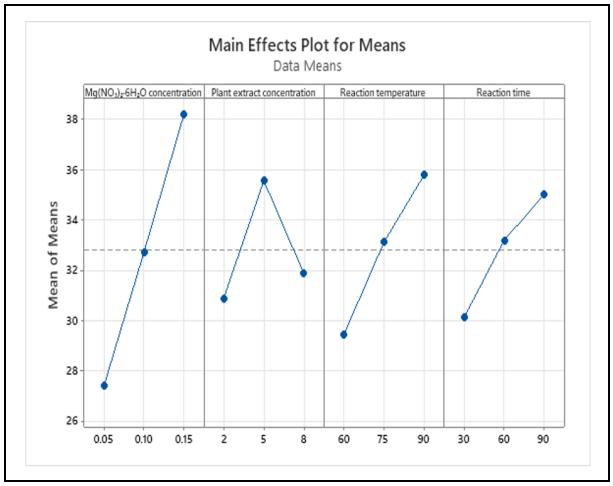

Fig. 2: Main effects plot for means

Main effects plots of larger-is-better signal-to-noise (S/N) ratios for MgO nanoparticle yield under different synthesis conditions based on Taguchi L27 orthogonal array were illustrated in fig. 3.

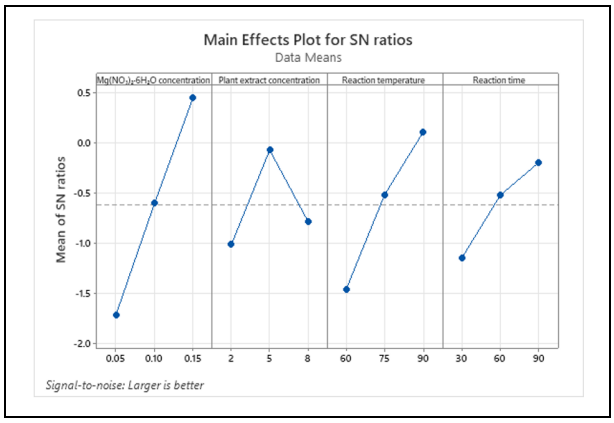

Fig. 3: Main effects plot for signal-to-noise (S/N) ratios

3.3 Analysis of Variance

ANOVA was performed to quantify contribution and statistical significance of the synthesis parameters. The ANOVA outcomes for MgO nanoparticle yield were presented in Table 5.

Table 5. ANOVA for MgO nanoparticle yield

Source	DF	Seq. SS	Contribution (%)	Adj. SS	Adj. MS	F-value	p-value
$Mg(NO_3)_2 \cdot 6H_2O$ concentration	2	2053.70	55.51	2053.70	1026.85	274.45	<0.001
Plant-extract concentration	2	428.96	11.59	428.96	214.48	57.32	<0.001
Reaction temperature	2	721.88	19.51	721.88	360.94	96.47	<0.001
Reaction time	2	428.06	11.57	428.06	214.03	57.21	<0.001
Error	18	67.35	1.82	67.35	3.74	—	—
Total	26	3699.95	100.00	—	—	—	—

All four synthesis factors significantly affected MgO nanoparticle yield, as indicated by p-values below 0.001. Magnesium nitrate concentration was the dominant factor, accounting for 55.51% of the total variation. Reaction temperature contributed 19.51%, whereas plant-extract concentration and reaction time contributed 11.59 and 11.57%, respectively. The residual contribution was only 1.82%, showing that the selected factors explained most of the observed yield variation.

The high F-value of 274.45 for magnesium nitrate concentration confirms that changes in precursor concentration produced a much larger effect than random experimental error. Reaction temperature also showed a strong influence, with an F-value of 96.47.

Magnesium nitrate concentration was also the largest contributor to UV–Vis absorbance, explaining 52.96% of total variation. Reaction temperature contributed 26.37%, followed by plant-extract concentration at 9.68% and reaction time at 9.30%. All parameters were statistically significant at $p < 0.001$.

The similar factor-ranking patterns obtained for yield and absorbance indicate that both responses were governed by related physicochemical processes. In particular, precursor availability and thermal conditions substantially controlled MgO nanoparticle formation.

3.4 LEBM-based Objective Weighting

The LEBM procedure assigned objective weights to MgO nanoparticle yield and UV–Vis absorbance. The calculated logarithmic effects and weights are presented in Table 7.

Table 6. ANOVA for UV–Vis absorbance

Source	DF	Seq. SS	Contribution (%)	Adj. SS	Adj. MS	F-value	p-value
$Mg(NO_3)_2 \cdot 6H_2O$ concentration	2	0.122732	52.96	0.122732	0.061366	282.65	<0.001
Plant-extract concentration	2	0.022434	9.68	0.022434	0.011217	51.66	<0.001
Reaction temperature	2	0.061102	26.37	0.061102	0.030551	140.71	<0.001
Reaction time	2	0.021554	9.30	0.021554	0.010777	49.64	<0.001
Error	18	0.003908	1.69	0.003908	0.000217	—	—
Total	26	0.231729	100.00	—	—	—	—

Table 7. LEBM objective weights

Criterion	LEBM Weight	Weight Rank
MgO nanoparticle yield	0.49821	2
UV–Vis absorbance	0.50179	1

The two criteria received nearly equal weights. UV–Vis absorbance was assigned a slightly greater weight of 0.50179, while MgO nanoparticle yield received a weight of 0.49821. The near-equal weights indicate that the LEBM analysis assigned comparable objective importance to both responses based on their information contribution within the experimental dataset. The small difference between the weights indicates that neither response disproportionately influenced the decision-making process. Consequently, both criteria contributed almost equally to the subsequent MARCOS ranking, enabling a balanced evaluation of the experimental alternatives.

3.5 MARCOS Ranking of Experimental Alternatives

The LEBM weights were incorporated into the MARCOS procedure to rank the 27 experimental alternatives. Both MgO yield and UV–Vis absorbance were treated as benefit criteria because larger values were desirable.

Table 8. MARCOS ranking of the experimental runs

Rank	Run	MgO Yield (%)	UV–Vis Absorbance (a.u.)
1	9	85.33	0.829
2	15	82.98	0.814
3	21	81.06	0.800
4	6	81.24	0.790
5	24	79.43	0.764
6	12	78.37	0.769
7	8	71.99	0.730
8	14	70.74	0.718
9	5	70.25	0.702
10	27	69.04	0.703
11	20	68.71	0.704
12	23	69.68	0.683
13	18	67.53	0.676
14	11	66.58	0.677
15	13	61.08	0.643
16	4	60.03	0.628
17	26	59.88	0.626
18	7	59.05	0.626
19	19	56.98	0.617
20	22	58.39	0.601
21	17	57.51	0.598
22	3	55.77	0.591
23	10	55.05	0.584
24	25	49.68	0.556
25	16	48.23	0.526
26	2	47.86	0.528
27	1	40.00	0.469

Therefore, Run 9 was identified as the best experimental run among the 27 tested conditions and should be distinguished from the Taguchi-predicted optimum obtained from the factor-level main-effects analysis.

The ranking generally increased with increasing precursor concentration and temperature. However, run 15, containing 5% extract, ranked above several conditions containing 8% extract. This supports the Taguchi observation that an intermediate concentration of *Mimusops elengi* extract can provide a favorable balance between phytochemical availability and reaction efficiency.

3.6 Artificial Neural Network Performance

The ANN model was evaluated by five-fold cross-validation. The predicted and experimental responses are shown in Fig. 4.

Table 9. Five-fold cross-validation performance of ANN

Response	(R^2)	RMSE	MAE	MAPE (%)
MgO nanoparticle yield	0.9642	2.2146	1.5936	2.62
UV–Vis absorbance	0.9644	0.0175	0.0119	1.89

The ANN produced R^2 values of 0.9642 and 0.9644 for MgO yield and UV–Vis absorbance, respectively. Most predicted values were located close to the identity line, indicating that the network captured nonlinear relationship among synthesis parameters and both responses. The slightly greater scatter observed at intermediate response levels may be attributed to limited sample size and nonlinear influence of plant-extract concentration.

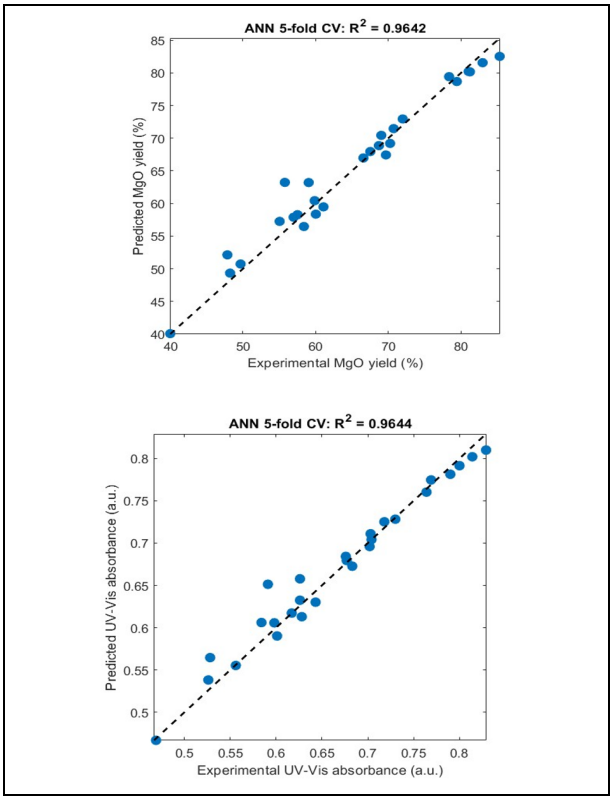

Fig. 4: Experimental versus ANN-predicted values obtained through five-fold cross-validation for (a) MgO nanoparticle yield and (b) UV–Vis absorbance

3.7 LSBoost Performance

LSBoost showed different predictive abilities for the two responses.

Table 10. Five-fold cross-validation performance of LSBoost

Response	R^2	RMSE	MAE	MAPE (%)
MgO nanoparticle yield	0.8775	4.0970	2.2743	4.22
UV–Vis absorbance	0.9708	0.01583	0.01125	1.66

For MgO yield, the LSBoost model achieved an R^2 of 0.8775, which was lower than those obtained using ANN and SVR. Several predictions in the low-to-intermediate yield range deviated visibly from the identity line. In contrast, LSBoost predicted UV–Vis absorbance accurately, with an R^2 of 0.9708. These results indicate that the LSBoost model captured the relationship between the MgO synthesis variables and the corresponding nanoparticle yield and UV–Vis absorbance responses, although its predictive performance differed between the two responses. The difference between its near-perfect training performance and lower cross-validated yield performance suggests that LSBoost partially overfitted the small dataset. Consequently, training statistics alone were not used to select the final predictive model (Fuloria *et al.* 2026).

The difference between its near-perfect training performance and lower cross-validated yield performance suggests that LSBoost partially overfitted the small dataset. Consequently, training statistics alone were not used to select the final predictive model.

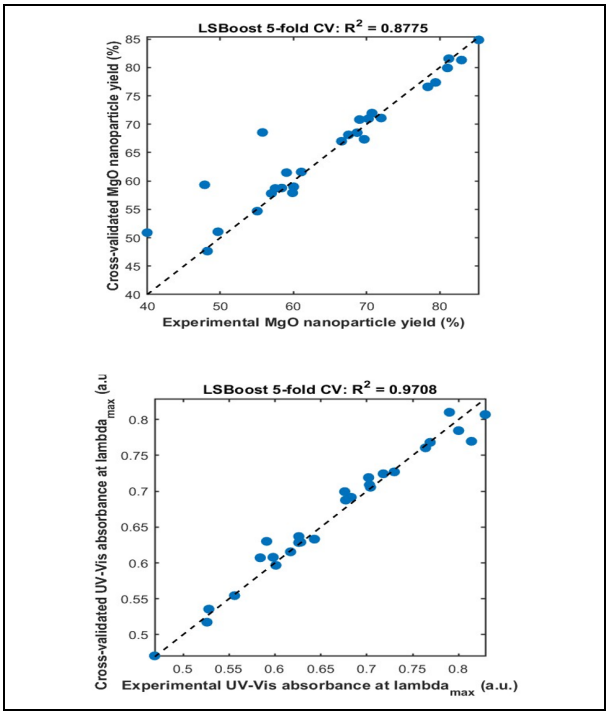

Fig. 5: Experimental versus LSBoost-predicted values obtained through five-fold cross-validation for (a) MgO nanoparticle yield and (b) UV–Vis absorbance

3.8 Support Vector Regression Performance

Among the initially compared models, SVR provided the most balanced predictive performance.

Table 11. Initial five-fold cross-validation performance of SVR

Response	R^2	RMSE	MAE	MAPE (%)
MgO nanoparticle yield	0.9762	1.8071	1.4856	2.35
UV–Vis absorbance	0.9758	0.0144	0.0118	1.80

The SVR prediction points were closely distributed along the 1:1 reference line for both responses. Its Gaussian kernel efficiently represented the nonlinear response surface without the stronger overfitting observed for LSBoost.

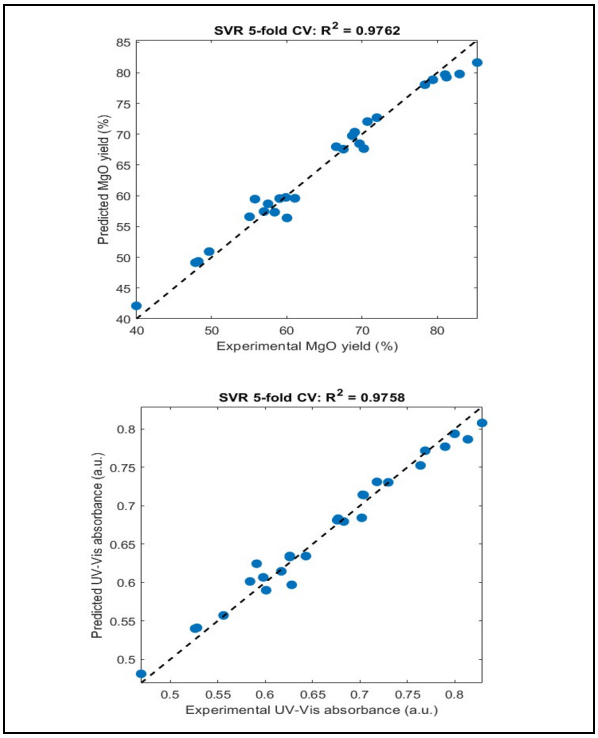

Fig. 6: Experimental versus SVR-predicted values obtained through five-fold cross-validation for (a) MgO nanoparticle yield and (b) UV–Vis absorbance

3.9 Comparative Assessment of Machine-learning Models

Table 12. Comparison of ANN, LSBoost and SVR models

Model	Yield CV-R^2	Absorbance CV- R^2	Mean CV-R^2
ANN	0.9642	0.9644	0.9643
LSBoost	0.8775	0.9708	0.9242
SVR	0.9762	0.9758	0.9760

SVR exhibited the highest average cross-validated R^2, while also maintaining low RMSE, MAE, and MAPE values. It was therefore selected for final tuning and process optimization.

Table 13. Performance of the final tuned SVR models

Response	CV-R^2	CV-RMSE	CV-MAE	CV-MAPE (%)	Full-data R^2
MgO nanoparticle yield	0.9841	1.4746	1.2706	2.04	0.9994
UV–Vis absorbance	0.9955	0.00623	0.00533	0.81	0.9996

The final SVR model explained 98.41% of the cross-validated variation in yield and 99.55% of the variation in absorbance. The low MAPE values indicate that the mean relative prediction errors were only 2.04% and 0.81%, respectively. The full-data R^2 values approached unity; however, the cross-validation values provide a more reliable measure of model generalization.

Despite the high predictive performance of the ML models, the dataset consisted of only 27 experimental observations. Therefore, the very high R^2 values, particularly those exceeding 0.999, should be interpreted cautiously because of the potential risk of overfitting. Although five-fold cross-validation was employed to assess predictive performance, the limited dataset restricts broader model generalizability. Further validation using a larger independent dataset is recommended in future studies.

3.10 SVR-based Process Optimization

The final SVR models were coupled with a multi-response desirability function to maximize MgO nanoparticle yield and UV–Vis absorbance simultaneously.

Table 14. SVR-predicted optimum conditions

Parameter	Optimized Value	Experimental Value
$Mg(NO_3)_2 \cdot 6H_2O$ concentration	0.14698 M	0.147 M
Mimusops elengi extract concentration	4.56378% w/v	4.56% w/v
Reaction temperature	87.735 °C	88 °C
Reaction time	85.905 min	86 min
Predicted MgO yield	86.1013%	—
Predicted absorbance	0.83324 a.u.	—
Overall desirability	1.0000	—

The optimized precursor concentration was close to the upper experimental level, consistent with the Taguchi and ANOVA findings that magnesium nitrate concentration was the most influential parameter. In contrast, the optimized extract concentration was intermediate, at approximately 4.56% w/v. This agrees with the main-effects analysis, which indicated that 5% extract produced a higher average response than either 2 or 8%.

The optimized temperature and time were close to their upper bounds, indicating that elevated thermal energy and sufficient reaction duration favored conversion of magnesium precursor into MgO nanoparticles.

The predicted yield of 86.10% was slightly greater than the best experimental yield of 85.33%, while the predicted absorbance of 0.83324 a.u. was marginally higher than the highest observed value of 0.829 a.u. These small improvements are reasonable because the SVR optimizer identified a continuous condition between the discrete Taguchi levels. In previous study states that, graphene-based microwave ablation applicators were designed and optimized using SVR and ANN models integrated with the Taguchi method, enabling accurate prediction (Singh and Yadav, 2024).

3.11 Experimental Confirmation

The SVR-predicted optimum was experimentally validated through three independent confirmation experiments conducted under the optimized conditions. The results were expressed as mean ± standard deviation (SD) and compared with the corresponding SVR-predicted values. Prediction error was calculated to quantify the agreement between the predicted and experimental responses.

Table 15. Experimental confirmation of the SVR optimum

Response	SVR-predicted value	Experimental mean ± SD	Residual	Prediction error (%)
MgO nanoparticle yield	86.1013%	85.267 ± 0.160%	−0.8347	0.9789
UV–Vis absorbance	0.83324 a.u.	0.82867 ± 0.00252 a.u.	−0.00457	0.5513

The experimental mean yield was 85.267%, compared with the predicted value of 86.1013%, resulting in an error of only 0.98%. Similarly, the experimental absorbance of 0.82867 a.u. differed from the predicted value by only 0.55%. Both errors were below 1%, indicating good agreement between the SVR-predicted and experimental values under the tested conditions. However, as validation was limited to triplicate confirmation experiments, additional independent experiments are required to establish broader predictive reliability.

3.12 Integrated Interpretation of Taguchi, ANOVA, MCDM and Machine Learning

The Taguchi, ANOVA, LEBM–MARCOS, and machine-learning analyses provided complementary information. Taguchi analysis identified the factor-level trends, while ANOVA quantified the contribution and significance of each synthesis variable. Magnesium nitrate concentration was consistently identified as the dominant factor for both responses, followed by reaction temperature.

The LEBM method allocated nearly equal weights to yield and absorbance, allowing both criteria to contribute comparably to the MARCOS ranking. MARCOS ranked the 27 discrete Taguchi experimental combinations and identified Run 9 (0.15 M precursor, 8% extract, 90 °C, and 90 min) as the best tested alternative. In contrast, the SVR model enabled continuous prediction within the investigated factor ranges and identified a continuous optimum at 0.14698 M precursor, 4.56378% extract, 87.735 °C, and 85.905 min. Thus, Run 9 represents the best discrete experimental condition, whereas the SVR solution represents the model-predicted continuous optimum.

Among the evaluated prediction methods, SVR demonstrated the best generalization. The complementary findings from Taguchi, ANOVA, MARCOS, and SVR provide a comprehensive interpretation of the synthesis process while reflecting the different purposes of discrete experimental ranking and continuous model-based optimization.

3.13 Characterization of MgO After Optimization

3.13.1 Visual Observation

Progress of MgO synthesis was initially monitored through visual observation of the reaction mixture. Following the addition of *Mimusops elengi* leaf extract to the magnesium nitrate hexahydrate solution under the optimized synthesis conditions, the initially transparent solution gradually became turbid, forming a milky-white suspension. As the reaction progressed, a white precipitate was observed, providing only a preliminary visual indication of magnesium-containing product formation. Visual observation alone was not considered sufficient to confirm MgO nanoparticle formation; the crystalline MgO phase was subsequently evaluated using XRD, while SEM was employed for morphological characterization.

3.13.2 UV–Vis Spectroscopic Analysis

The synthesized MgO nanoparticles were characterized by UV–Vis spectroscopy to evaluate their optical characteristics. The absorption spectrum exhibited a characteristic band in the ultraviolet region, with an absorption maximum at approximately 375–380 nm (Fig. 7). Time-dependent spectra recorded after 1, 2, and 4 h were used only to examine the evolution of optical absorption during a preliminary study observation. These measurements were not used to define the Taguchi reaction-time levels. For the optimization study, reaction times of 30, 60, and 90 min were independently selected and evaluated according to the Taguchi L27 design. Therefore, the 4 h spectrum represents an extended monitoring point and should not be interpreted as the reaction completion time used in the optimization experiments.

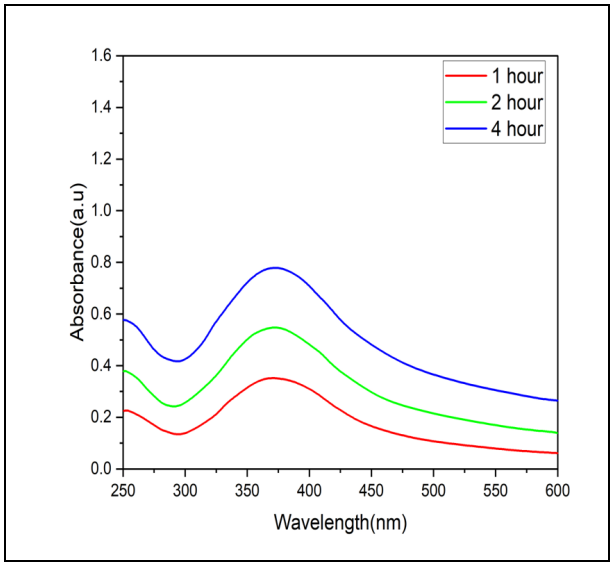

Fig. 7: UV–Vis absorbance during MgO synthesis

UV–Vis absorbance was used as a comparative optical response rather than as a direct quantitative measure of MgO nanoparticle yield. To ensure comparability among experimental runs, the samples were analysed under identical dispersion, sample volume, cuvette path length, wavelength range, and instrumental conditions. The absorbance measured at the characteristic absorption maximum was used as the optimization response. Therefore, variations in absorbance were interpreted comparatively under standardized measurement conditions.

3.13.3 X-ray Diffraction Analysis

The crystal structure of the synthesized MgO were examined by X-ray diffraction (XRD) over a 2θ range of 5°–100°. The obtained diffraction pattern is presented in Fig. 8. The XRD profile exhibited distinct reflections at 2θ values of 31.2°, 35.2°, 44.9°, 62.1°, and 73.2°. The experimentally observed reflections were compared with the reference diffraction pattern of cubic MgO using JCPDS card No. 45-0946. No prominent additional crystalline reflections were observed within the detection limits of the XRD measurement, suggesting the absence of major secondary crystalline phases.

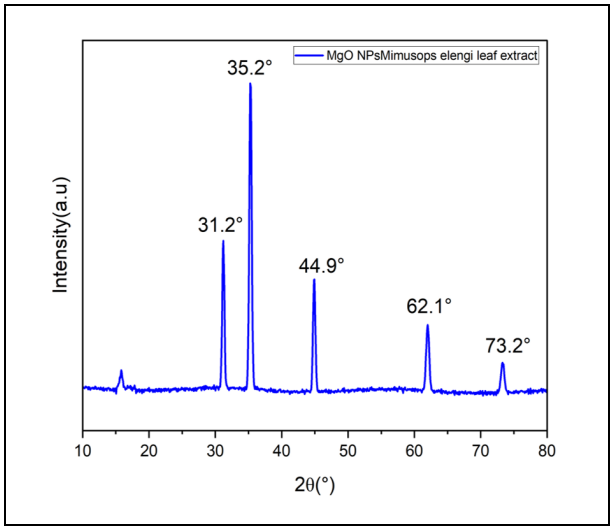

Fig. 8: X-ray diffraction pattern of MgO nanoparticles synthesized using *Mimusops elengi* leaf extract

The average crystallite size was estimated using the Debye–Scherrer equation (Eq. 25) from the most intense diffraction peak and was approximately 20 nm. The calculated value represents the coherent crystalline-domain size and should not be interpreted as the physical particle size observed by SEM. Since instrumental broadening was not independently corrected, the calculated crystallite size should be considered an approximate estimate (Villarta *et al.* 2025).

$$D = \frac{0.9\lambda}{W\mathrm{Cos}\theta} \quad \ldots (25)$$

3.13.4 SEM Analysis

Surface morphology of synthesized MgO nanoparticles obtained under the optimized preparation conditions was examined by scanning electron microscopy, and the corresponding micrographs were presented in Fig. 9.

SEM characterization was performed on both the SVR-optimized and Taguchi–MCDM-selected samples to qualitatively compare their resulting surface morphologies under the two optimized synthesis conditions (Fig. 10). Morphology was not included as an optimization response; the optimization was based exclusively on MgO nanoparticle yield and UV–Vis absorbance. Therefore, the SEM comparison was intended only as a post-optimization morphological assessment and not as validation of the optimization models.

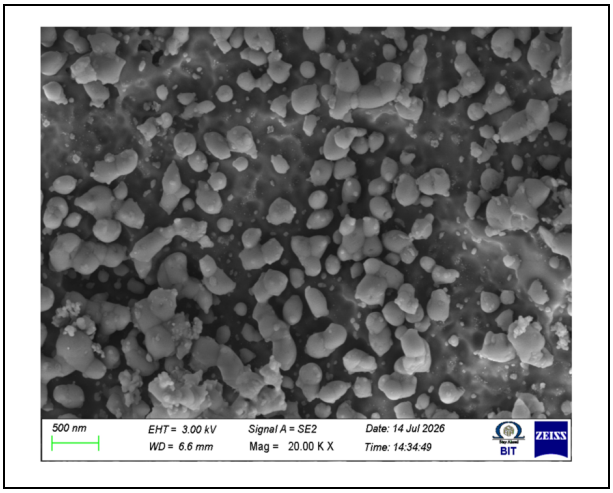

Fig. 9: SEM image of MgO nanoparticles synthesized by *Mimusops elengi*

Surface morphology was characterized using a ZEISS Gemini scanning electron microscope. The dried MgO samples were ultrasonically dispersed in double-distilled water, drop-cast onto conductive carbon adhesive tape, and dried at room temperature. SEM micrographs were acquired at a magnification of 4.00 k× using an accelerating voltage of 3.00 kV. The SEM micrographs of samples synthesized under the SVR-predicted optimum (Fig. 10a) and Taguchi–MCDM-selected conditions (Fig. 10b) are presented in Fig. 10. Both samples exhibited irregular granular features with varying degrees of aggregation. The SVR-optimized sample showed relatively coarse aggregates associated with larger flake-like structures, whereas the Taguchi–MCDM-selected sample exhibited a comparatively more uniform distribution of nearly spherical-to-irregular features. However, these observations were used only for qualitative morphological comparison. Quantitative particle-size distribution was not determined from multiple SEM fields in the present study. The crystallite size of approximately 20 nm estimated from XRD represents the coherent crystalline domain size and should not be interpreted as the physical particle size observed by SEM. The SEM-observed features and aggregates may comprise multiple crystallites. Quantitative particle-size analysis using multiple SEM images is recommended for future investigation.

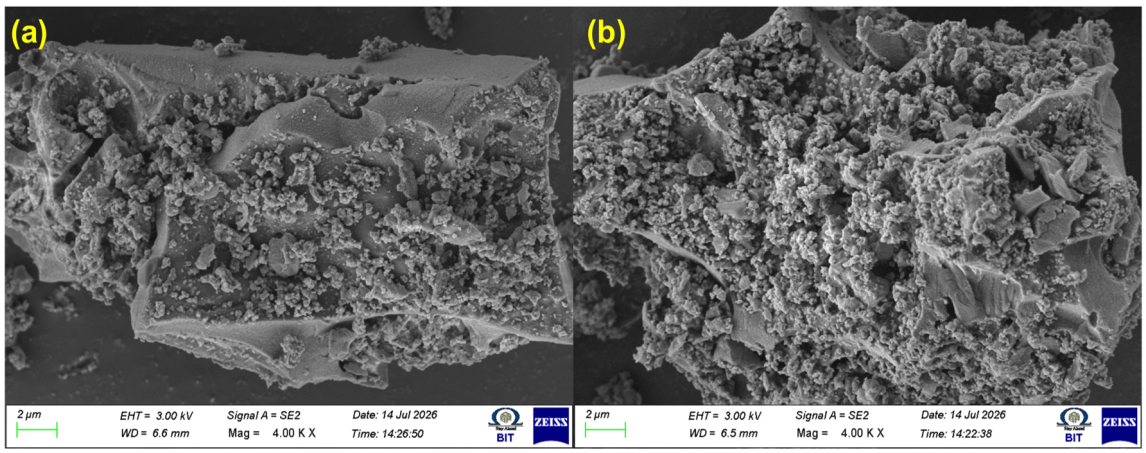

Fig. 10: SEM image comparison of MgO nanoparticles synthesized under (a) SVR-predicted optimum conditions and (b) Taguchi–MCDM-selected conditions

4. CONCLUSION

This research demonstrated the green synthesis and optimization of MgO nanoparticles using *Mimusops elengi* leaf extract and magnesium nitrate hexahydrate through a Taguchi-assisted experimental design. Among the investigated synthesis variables, magnesium nitrate concentration was identified as the most influential factor affecting MgO nanoparticle yield and UV–Vis absorbance, followed by reaction temperature, while plant-extract concentration and reaction time showed comparatively smaller effects. The LEBM–MARCOS approach ranked the experimental conditions by considering both responses simultaneously. MARCOS identified Run 9 as the best discrete experimental alternative, whereas SVR identified a continuous model-predicted optimum within the investigated factor ranges.

The predictive performance of the ANN, LSBoost, and SVR models was systematically evaluated using five-fold cross-validation. Among these models, SVR showed the best overall predictive performance, with cross-validated R^2 values of 0.9841 for MgO yield and 0.9955 for UV–Vis absorbance. The SVR-predicted optimum conditions (0.147 M magnesium nitrate, 4.56% *Mimusops elengi* extract, 88 °C, and 86 min) resulted in a predicted MgO yield of 86.10% and UV–Vis absorbance of 0.833 a.u., with triplicate confirmation experiments showing prediction errors below 1%. However, because the ML models were developed using only 27 experimental observations, these predictive results should be interpreted cautiously, and validation using larger independent datasets is required to establish broader generalizability.

XRD supported the presence of crystalline MgO with an estimated crystallite size of approximately 20 nm, while SEM provided qualitative information on surface morphology. UV–Vis absorbance served as a comparative optical response under standardized measurement conditions. Overall, the integrated Taguchi–ANOVA–LEBM–MARCOS–SVR approach provided a useful optimization framework for the investigated MgO synthesis system. Its applicability to other sustainable nanomaterial synthesis processes should be explored and validated in future studies.

FUNDING

This research received no specific grant from any funding agency in the public, commercial, or not-for-profit sectors.

CONFLICTS OF INTEREST

The authors declare that there is no conflict of interest.

COPYRIGHT

This article is an open-access article distributed under the terms and conditions of the Creative Commons Attribution (CC BY) license (http://creativecommons.org/licenses/by/4.0/).

REFERENCES

Altıntaş, F. F., A new approach for determining weight coefficients of criteria within the scope of multi-criteria decision making: Logarithmic effect-based measurement (LEBM), *J. Turkish Operat. Manage.*, 9(1), 215–232 (2025). https://doi.org/10.56554/jtom.1327595

Anh, N. T. K., Thai, N. X., Chinh, N. T., Trung, V. Q., Thuy, T. T. and Hoang, T., Optimization of synthesizing silver nanoparticles on hydrotalcite-zinc using a piper betle leaf extract as a reducing agent, *Vietnam J. Chem.*, 63(3), 451–461 (2025). https://doi.org/10.1002/vjch.202400152

Babu, B., Manikandan, M., Yadav, S. K., Nithyanandhan, T., Vijayasekaran, G., Kumar, K. S. and Seenivasan, S., Influence of silicon dioxide nanoparticles on the mechanical and moisture-resistance behavior of roselle fiber–reinforced epoxy composites: a CRITIC–MARCOS evaluation, *Interact.*, 247(1), 143 (2026). https://doi.org/10.1007/s10751-026-02501-1

Blessymol, B., Kalaiselvi, V., Yasotha, P. and Gopi, S., Comparative Study of Chemically and Green Synthesized Titanium Dioxide Nanoparticles using Leucas aspera Leaf Extract, *J. Environ. Nanotechnol.,* 12(3), 10-13 (2023). https://doi.org/10.13074/jent.2023.09.233471

Edlabadkar, A. P., Madhu, M. C., Arunbharathi, R., Sharma, D., Singh, N., Revathi, R. and Mayakannan, S., Optimization of Mechanical Properties of Cordia dichotoma/Alumina Nanoparticle Reinforced Epoxy Nanocomposites Under Alkali Treatment Using ANN Techniques, *J. Environ. Nanotechnol.*, 14(2), 525–540 (2025). https://doi.org/10.13074/jent.2025.06.2521549

Fuloria, D., Cherian, C. B., Sathees Kumar, S., Borkar, S. V. S., Manikandan, Y., Giri, A., Pati, P. R., Purohit, A. and Gupta, G., Machine learning based prediction on mechanical and wear characterization of sisal fiber reinforced dolomite dust-epoxy hybrid composites, *J. Mater. Res. Technol.*, 41, 3107–3132 (2026). https://doi.org/10.1016/j.jmrt.2026.01.210

Gomkale, S. A., Stephen, M., Mayakannan, S., Suresh, R., Kumar, K. R. and Vinukumar, K., Performance and Emission Optimization of Spirulina platensis Biodiesel Blends with Green-synthesized CeO_2 Nanoparticles for Low-emission Diesel Engines, *J. Environ. Nanotechnol.*, 15(2), 512–529 (2026). https://doi.org/10.13074/jent.2026.06.2622134

Gomkale, S., Khamaj, A., Ali, A. M., Saminathan, R., Satishkumar, P., Naga Swapna Sri, M., Gupta, D. and Sivasundar, V., Synergistic effects and optimization of surface-modified borassus and madar fibers in hybrid epoxy composites with lotus seed powder filler, *J. Ceram. Proce. Res.*, 26(6), 1009–1023 (2025). https://doi.org/10.36410/jcpr.2025.26.6.1009

Hossain, S., Jalil, M. A., Islam, T., Mahmud, R. U., Kader, A. and Islam, M. K., Enhancement of antibacterial and UV protection properties of blended wool/acrylic and silk fabrics by dyeing with the extract of *Mimusops elengi* leaves and metal salts, *Heliyon*, 10(3), e25273 (2024). https://doi.org/10.1016/j.heliyon.2024.e25273

Jang, Y., Choi, Y. and Bhakta, S., Prediction of VRFB state of health in PV-coupled systems using PSO-optimized ensemble and neural models, *Comp. Chem. Eng.*, 210, 109632 (2026). https://doi.org/10.1016/j.compchemeng.2026.109632

Jeevanandam, J., Chan, Y. S. and Micheal, D. K., Biosynthesis and Characterization of MgO Nanoparticles from Plant Extracts via Induced Molecular Nucleation, *New J. Chem.*, 41(7), 2800–2814 (2017). https://doi.org/10.1039/C6NJ03176E

Kar, A., Deole, S., Gadratagi, B. G., Patil, N., Guru-Pirasanna-Pandi, G., Mahanty, A., Mahapatra, B., Gupta, A. K., Das Mohapatra, S. and Adak, T., Biogenic magnesium oxide-rice husk biochar composite: synthesis, characterization, and optimization of pesticide sorption using response surface methodology, *Biomass Convers. Biorefine.*, 15(12), 18567–18583 (2025). https://doi.org/10.1007/s13399-024-06469-2

Khanam, S., Khan, O., Ahmad, S., Sherwani, A. F., Khan, Z. A., Yadav, A. K. and Ağbulut, Ü., A Taguchi-based hybrid multi-criteria decision-making approach for optimization of performance characteristics of diesel engine fuelled with blends of biodiesel-diesel and cerium oxide nano-additive, *J. Therm. Anal. Calorim.*, 149(8), 3657–3676 (2024). https://doi.org/10.1007/s10973-024-12918-x

Ogunsile, B. O., Okoh, O. S., Ejidike, I. P. and Omolaja, O. R., Biosynthesis and Optimization of AgNPs Yield from *Chromolaena Odorata* Leaf Extract Using Response Surface Methodology (RSM), *Phys. Chem. Res.*, 12(1), 21–31 (2024). https://doi.org/10.22036/pcr.2023.366212.2226

Packiam, K. K., Imdhiyas, M., Sabarivasan, K. and Madhankumar, D., Studies on Antioxidants, Antibacterial activities and Phytochemistry of *Mimusops elengi*. Linn, *Res, J, Biotechnol.*, 17(3), 27–32 (2022). https://doi.org/10.25303/1703rjbt2732

Periakaruppan, R., Ariuthayan, B., Vanathi, P., Selvaraj, K. S. V, Al-Dayan, N., Dhanasekaran, S. and Parthiban, A., Fabrication of Allium cepa–assisted magnesium oxide nanoparticles with antibacterial and antioxidant properties, *Biomass Convers. Biorefine.*, 15(15), 22491–22498 (2025a). https://doi.org/10.1007/s13399-023-04828-z

Periakaruppan, R., Monica Jannett, S., Vanathi, P., Selva Kumar, T. and Selvaraj, K. S. V., Phyto-synthesis, characterization of magnesium oxide nanoparticles using aqueous extract of Piper betle leaf and an assessment of its antioxidant potential, *Biomass Convers. Biorefine.*, 15(19), 26597–26604 (2025b). https://doi.org/10.1007/s13399-023-05116-6

Prisrin, S. A., Priyanga, M., Ponvel, K. M., Kaviarasan, K. and Kalidass, S., Plant Mediated Approach for the Fabrication of Nano CuO–NiO Mixed Oxides Using Aqueous Extract of *Mimusops elengi* Leaf: Green Synthesis, Characterization and Antibacterial Activity Studies, *J. Clust. Sci.*, 33(2), 765–772 (2022). https://doi.org/10.1007/s10876-021-02016-5

Ramadhan, R. A. and Ahmed, S. M., Influence of Precursor Concentration on Structural and Morphological Properties of Eco-Friendly Synthesized Magnesium Oxide Nanoparticles, *Iraqi J. Appl. Phy*., 22(3), 413–421 (2026).

Roy, C. S., Gupta, U., Kumari, M., Thakur, S., Lata, A., Kumar, N., Gandhi, S. and Arun, R. K., Green-synthesis of Murraya koenigii carbon dots integrated with rGO for electrochemical detection of creatinine in human urine samples, *Indus. Crops Prod.*, 234, 121625 (2025). https://doi.org/10.1016/j.indcrop.2025.121625

Silva, A. A., Sousa, A. M. F., Furtado, C. R. G. and Carvalho, N. M. F., Green magnesium oxide prepared by plant extracts: synthesis, properties and applications, *Mater. Today Sustain.*, 20, 100203 (2022). https://doi.org/10.1016/j.mtsust.2022.100203

Singh, S. K. and Yadav, A. N., Advancing microwave ablation applicators: integrating computational modeling of a graphene-based applicator with machine learning for ablation zone prediction, *J. Computat. Electron.*, 23(4), 832–850 (2024). https://doi.org/10.1007/s10825-024-02186-1

Sonya, A., Kalarani, P., Maheskumar, P., Selvam, P. M. S., Sathish, M., Vimalanathan, P. and Mayakannan, S., Optimization of Tensile Strength in Nano Silica and Calotropis Gigantea Reinforced Hybrid Polymer Nanocomposites using ANN-BBD Modelling, *Int. J. Veh. Struct. Syst.*, 17(4), 680–688 (2025). https://doi.org/10.4273/ijvss.17.4.22

Tariq, A., Yousaf, Z., Aftab, A. and Maqbool, Z., Effect of Magnesium Oxide Nanoparticles Synthesized from Malus domestica Borkh. on Shelf Life of Spinacia oleracea L., *J. Food Process Eng.*, 49(6), e70581 (2026). https://doi.org/10.1111/jfpe.70581

Tero, T. K., Debela, S., Abera, W. G. and Gebreyes, D. A., An eco-friendly, plant-mediated synthesis of antibacterial magnesium oxide nanoparticles using Vernonia amygdalina (bitter leaf), *J. Environ, Sci. Health - Part A,* 61(8), 619–634 (2026). https://doi.org/10.1080/10934529.2026.2670142

Thai, N. X., Chinh, N. T., Linh, B. T., Thuy, T. T. and Hoang, T., Optimizing Green Synthesis of Hydrotalcite – Silver Nanoparticles using Syzygium Nervosum based Reducing Agent, *Chem. An Asian J.*, 19(14), e202400162 (2024). https://doi.org/10.1002/asia.202400162

Ulwali, R. A., Abass, N. K., Majed, M. D. and Alwally, H. A., Green synthesis of mgo nps by olea europeae leaves extract from bulk mgo and study physical properties, *Neuro Quantol.*, 19(5), 114–119 (2021). https://doi.org/10.14704/nq.2021.19.5.NQ21055

Villarta, J. D. A., Paylago, F. J. C., Poldo, J. C. H., Santos, J. S. R., Escordial, T. A. M. M. and Montealegre, C. M., Green Synthesis, Characterization, and Optimization of Chitosan Nanoparticles Using Blumea balsamifera Extract, *Proce.*, 13(3), 804 (2025). https://doi.org/10.3390/pr13030804